Singular value analysis of the Jacobian matrix in microwave image reconstruction

Qianqian Fang, Paul M. Meaney, *Member, IEEE,* and Keith D. Paulsen, *Member, IEEE*

***Abstract*— For non-linear inverse scattering problems utilizing Gauss-Newton methods, the Jacobian matrix encodes rich information concerning the system performance and algorithm efficiency. In this paper, we perform an analytical evaluation of a single-iteration Jacobian matrix based on a previously derived nodal adjoint representation. Concepts for studying linear ill-posed problems, such as the degree-of-ill-posedness, are used to assess the impact of important system parameters on the expected image quality. Analytical singular value decomposition (SVD) of the Jacobian matrix for a circular imaging domain is derived along with the numerical SVD for optimizing imaging system configurations. The results show significant reductions in the degree-of-ill-posedness when signal frequency, antenna array density and property parameter sampling are increased. Specifically, the decay rate in the singular spectrum of the Jacobian decreases monotonically with signal frequency being approximately $\frac{1}{3}$ of its 0.1GHz value at 3GHz, is improved with antenna array density up to about 35 equally-spaced circumferentially positioned elements and drops significantly with increased property parameter sampling to more than twice the amount of measurement data. These results should serve as useful guidelines in the development of design specifications for an optimized hardware installation.**

***Index Terms*— Jacobian matrix, microwave imaging, singular value analysis, Zernike polynomial**

I. Introduction

For inverse scattering problems involving high-contrast or large targets, reconstruction methods based on linear assumptions such as the Born or Rytov approximations [1] are insufficient to produce accurate solutions [2]. In these situations, iterative approaches, for example the distorted Born [3] and Gauss-Newton methods [4], [5] (proven to be equivalent in [6]) are more appropriate in correctly accounting for the nonlinearity in the electromagnetic property-field relationship. Microwave tomographic imaging [7] recovers the dielectric properties, i.e. the permittivity and conductivity, by interrogating the region of interest with microwave signals and utilizing the measured response to estimate the property distribution. Microwave imaging is seemingly a very promising alternative to traditional medical modalities because it is non-ionizing and the biological tissue can present far greater normal/malignant property contrasts [8]. As a consequence of the high-contrast, iterative image reconstruction is needed to recover the dielectric property distributions in various microwave imaging applications [7], [9]–[15].

Iterative microwave image reconstruction essentially converts the nonlinear problem into a series of linearized steps. The unknown dielectric properties are initialized by a reasonable estimate and are updated iteratively based on solutions to a linearized property-field relationship [5]. Consequently, the equation producing the updates plays a central role in the reconstruction process. Specifically, the final image is governed by the series of solutions generated from this equation over the sequence of iterations. In the case of Gauss-Newton, the update equation involves the measurement data, parameter update and a sensitivity map in the form of the Jacobian matrix. Analysis of the update equation, especially the Jacobian matrix, is of great importance in understanding the behavior of the reconstructor and assessing the performance of the imaging system. More importantly, these insights may be useful in optimizing the measurement system. The principal questions we are interested in exploring with this analysis include:

1) Identification of the metrics that reasonably characterize the performance of the imaging scheme.
2) Assessment of the resolution limits and the factors that impact it.
3) Assessment of the influence of measurement noise on the final image.
4) Optimization of system parameters (such as operating frequency, source/detector number and spatial arrangement, etc.) that yield the highest image quality.

Because of the nonlinearity involved, analyzing the property update over the entire sequence of iterations is quite challenging. However, the update equation for one iteration can be explored quite conveniently. Although the single-iteration update equation is linear, it does provide a certain measure of the recoverability of the target for a given measurement configuration and associated inversion algorithm. Moreover, the overall performance of an iterative method can be reasonably inferred from the single-iteration analysis.

For a general linear system expressed as $A\mathbf{x} = \mathbf{b}$, singular value decomposition (SVD) of the left-hand-side matrix, A, has been shown to be a powerful tool for studying the internal structure of the coupled linear equations: the left singular vectors of A provide the basis set over which the right-hand-side vector, $\mathbf{b}$, is factored; the right singular vectors of A are the basis modes required to form the solution, $\mathbf{x}$; and the singular values, or the singular spectrum, of A provide a native measure for ranking the importance of these basis modes in solving the equation [16]–[18]. This decomposition

Manuscript received July 13, 2005. This work was supported in part by National Institutes of Health (NIH) through the National Cancer Institute under Grant P01-CA80139.

The authors are with Thayer School of Engineering, Dartmouth College, Hanover, NH 03755 USA (e-mail: qianqian.fang.th05@alum.dartmouth.org, paul.m.meaney@dartmouth.edu, keith.d.paulsen@dartmouth.edu)

Digital Object Identifier 00.0000/TAP.0000.000000

0000–0000/00$20.00 © 2005 IEEE

is especially advantageous when A is ill-conditioned, which is often the case in nonlinear image reconstruction where the mathematical problem is ill-posed. The conceptual simplicity of the SVD facilitates its increasing use in the theoretical analysis of linear ill-posed problems and its potential extrapolation to nonlinear systems. For imaging applications, Brander and DeFacio studied the SVD of the inverse Born operator for a single step reconstruction from a homogeneous background and far field assumption [19]. In their investigation, the SVD of the discretized inverse Born operator was computed using a generalized description. Hori also derived a reconstruction algorithm based on the SVD of the Green's matrix [20]. Bucci *et al.* studied the degrees-of-freedom for electromagnetic inverse scattering where the SVD of the forward operator was involved [21], [22]. For forward problems, Nelson and Kahana used the SVD of the Green's matrix to analyze the basic modes in terms of spherical harmonics in acoustic scattering problems [23].

In this work, we approach the SVD analysis of the Gauss-Newton reconstruction in tomographic microwave imaging in a similar vein to [19], i.e. we focus on the SVD of the single-step update equation from a homogeneous background estimate. However, there are several significant differences: 1) the decomposition process in our study is based on a discrete adjoint form of the Jacobian matrix as described in [24], 2) the near field imaging problem with localized source illumination is considered, 3) the analytical form of the decomposition which follows the process outlined in Nelson and Kahana [23] is explicit to single-domain microwave imaging, and 4) a numerical SVD analysis is presented to assess the impact of various system parameters including operating frequency, source/receiver number and background contrast on the singular spectrum of the sensitivity (Jacobian) matrix and by implication the expected image quality. The advantage of the approach is that we can quickly identify the influence of these parameters on the degree-of-illposedness, and hence, infer the likely image outcome without actually reconstructing complete images for each parameter set. This is a substantial savings in the time and effort required to explore the complete parameter range that would be necessary to fully characterize imaging performance. However, it is also important to recognize that changes in the singular spectrum cannot be directly related to image outcome measures such as spatial resolution because of the algorithmic complexities (i.e. nonlinearities) associated with the computational tasks involved.

In the remainder of this paper, a brief introduction to the Gauss-Newton update equation and construction of a discrete adjoint form of the Jacobian matrix is provided in Section II-A. In Section II-B, the analytical decomposition of a single-iteration Jacobian matrix is illustrated. Because a circular domain with equi-spaced antennas is frequently used for tomographic imaging, the analytical SVD for this case is discussed in Section II-C. For assessing the impact of different system configurations, a metric is constructed from the numerical singular value spectrum of the Jacobian matrix and is computed for a series of typical cases (Section III) to facilitate system parameter optimization. Conclusions from this study are summarized in Section IV.

II. Theory

A. Discrete adjoint form of the Jacobian matrix

The reconstruction problem in microwave imaging is essentially a nonlinear optimization. Using the least-square criterion, the form of the optimization can generally be expressed as

$$\min_{k^2(\vec{r})} \; ||E(\vec{r},\omega,k^2(\vec{r})) - E^{\text{meas}}(\vec{r},\omega)||_2^2 \tag{1}$$

where E is the computed electric field and E^{meas} is the field measurement, $\vec{r}$ denotes a spatial vector, ω is the operating frequency, $k^2(\vec{r}) = \omega^2\mu_0\epsilon_0\epsilon_r(\vec{r}) - j\omega\mu_0\sigma(\vec{r})$ is the squared complex wavenumber containing the unknown relative permittivity $\epsilon_r(\vec{r})$ and the unknown conductivity $\sigma(\vec{r})$ (assuming time-dependence $\exp(j\omega t)$). ϵ_0 and μ_0 are the permittivity and magnetic permeability of free space, respectively. $j = \sqrt{-1}$ is the imaginary unit.

Solving the optimization problem (1) with the Gauss-Newton method in conjunction with an appropriate discretization scheme, the update equation for the dielectric properties at the i-th iteration can be written in the form:

$$(J^TJ + \lambda I)(\mathbf{k}^2_{(i)} - \mathbf{k}^2_{(i-1)}) = J^T(\mathbf{E}_{(i)} - \mathbf{E}^{\text{meas}}) \tag{2}$$

where $\mathbf{E}$ (of length Q) and $\mathbf{k}^2$ (of length P) are the discretized vectors for electric field and dielectric property, respectively; J represents the Fréchet derivative between $\mathbf{E}$ and $\mathbf{k}^2$ and is referred to as the Jacobian matrix. The term J^TJ, called the Gauss-Hessian matrix, is ill-conditioned in most cases and the scalar constant λ multiplied by the identity matrix I is used to regularize the system to produce numerically meaningful solutions (this scheme is often referred to as the standard Tikhonov regularization for linear ill-posed problems).

Equivalently, (2) can be solved by the truncated SVD (TSVD) solution of the following equation

$$J(\mathbf{k}^2_{(i)} - \mathbf{k}^2_{(i-1)}) = \mathbf{E}_{(i)} - \mathbf{E}^{\text{meas}} \tag{3}$$

If the SVD of J can be constructed, the solution to (3) can then be obtained in a straightforward manner [18] by writing

$$J = U\Sigma V^T \tag{4}$$

where $U = \{\mathbf{u}_1, \mathbf{u}_2, \cdots, \mathbf{u}_P\} \in \mathbb{C}^{Q\times P}$ and $V = \{\mathbf{v}_1, \mathbf{v}_2, \cdots, \mathbf{v}_P\} \in \mathbb{C}^{P\times P}$ are both column orthogonal matrices, i.e. $U^HU = V^HV = I$. Σ is a diagonal matrix with non-negative real values arranged in decreasing order, i.e. $\Sigma = \text{diag}\left(\{\sigma_i\}_{i=1}^P\right)$ with $\sigma_1 \geq \sigma_2 \geq \cdots \geq \sigma_P \geq 0$. Vectors $\mathbf{u}_i$ and $\mathbf{v}_i$ are referred to as the i-th left and right singular vectors, respectively, while σ_i is the i-th singular value. The sequence $\{\sigma_1, \sigma_2, \cdots, \sigma_n\}$ is referred to as the singular spectrum of J.

In [25], we derived a discrete adjoint form of the Jacobian matrix over a general dual-mesh configuration based on finite element treatment of the underlying equations. By reconditioning the weighting matrices, we further obtained a more succinct, albeit slightly approximated, formula for computing the Jacobian matrix, i.e. the nodal adjoint method [24]. With this method, the Jacobian matrix for a point source imaging

system (discretized by linear Lagrange elements) can be written as

$$J((s,r),\tau) = \sum_{n\in\Omega_\tau} \left(\frac{\sum_{e\in\Omega_n} V_e}{M} \right) \varphi_\kappa(\vec{r}_n) E_s(\vec{r}_n) \hat{E}_r(\vec{r}_n) \tag{5}$$

where $J((s,r),\tau)$ is an element of J representing the sensitivity of the measurement at the r-th receiver with respect to perturbations of the τ-th property parameter under illumination from the s-th source. E_s and $\hat{E}_r$ are the associated field distributions with respect to illumination at the s-th source and the r-th receiver, respectively. Ω_τ is the spatial union of the parameter mesh elements which share the τ-th parameter node. $\sum_{n\in\Omega_\tau}$ refers to the summation over the field points (nodes in the field mesh associated with the finite element discretization) which fall inside Ω_τ whereas $\sum_{e\in\Omega_n}$ refers to the summation over the corresponding mesh elements that share the n-th field node. V_e is the element volume or area; M is the number of nodes per element. The term $\left(\frac{\sum_{e\in\Omega_n} V_e}{M}\right)$ is a scalar quantity associated with the n-th field node which can be rewritten as V_n and considered to be the effective volume of node n. It should be noted that this definition is essentially a weighted inner product of field distributions due to illuminations at the two antennas. This technique has been shown to be accurate and much more computationally efficient than previous computationally exact strategies [12], [25].

B. Analytical SVD of the Jacobian matrix

The nodal adjoint formula (5) provides a simple but meaningful representation of the Jacobian matrix. For a uniform single-mesh, i.e. where the field and property parameter meshes are identical and the nodes are evenly distributed (for each node, their effective volumes V_n ($n = 1, \cdots, P$) are approximately identical, denoted as V), the Jacobian matrix can be written as

$$J = VB \tag{6}$$

where the $((s,r),\tau)$-th element of matrix B is given by

$$b_{(s,r),\tau} = E(\vec{r}_\tau, \vec{r}_s)\hat{E}(\vec{r}_\tau, \vec{r}_r) \tag{7}$$

In (7), (s,r) represents a transmitter/receiver pair where s is the index of the source and r is the index of the receiver. τ is the index of the property parameter while $E(\vec{r}_\tau, \vec{r}_s)$ and $\hat{E}(\vec{r}_\tau, \vec{r}_r)$ are the electric fields at node τ due to sources at either $\vec{r}_s$ or $\vec{r}_r$, respectively. For simplicity, we use a single index ν to represent all possible (s, r) pairs and a one-to-one mapping is established [26] denoted as $\nu : \{1, 2, \cdots, Q\} \rightarrow (s,r)$ where Q is the total number of combinations. Thus, (7) can be re-written as

$$b_{\nu,\tau} = E(\vec{r}_\tau, \vec{r}_{\nu:s})\hat{E}(\vec{r}_\tau, \vec{r}_{\nu:r}) \tag{8}$$

where $\nu : s$ and $\nu : r$ are the corresponding source and receiver indices in the ν-th pair, respectively.

For the microwave imaging case, the receivers and sources are both represented as point elements, therefore, the field E_s and $\hat{E}_r$ can be expressed in terms of Green's functions, i.e.

$$\begin{aligned} E(\vec{r}, \vec{r}_{\nu:s}) &= \eta \times g(\vec{r}, \vec{r}_{\nu:s}) \\ \hat{E}(\vec{r}, \vec{r}_{\nu:r}) &= g(\vec{r}, \vec{r}_{\nu:r}) \end{aligned} \tag{9}$$

where η is a constant denoting the source strength. Substituting (9) into (7) and subsequently into (6), the Jacobian can be expressed as

$$J = \eta V \begin{pmatrix} g(\vec{r}_1, \vec{r}_{1:s})g(\vec{r}_1, \vec{r}_{1:r}) & g(\vec{r}_2, \vec{r}_{1:s})g(\vec{r}_2, \vec{r}_{1:r}) & \cdots & g(\vec{r}_P, \vec{r}_1 \\ g(\vec{r}_1, \vec{r}_{2:s})g(\vec{r}_1, \vec{r}_{2:r}) & g(\vec{r}_2, \vec{r}_{2:s})g(\vec{r}_2, \vec{r}_{2:r}) & \cdots & g(\vec{r}_P, \vec{r}_2 \\ \cdots & \cdots & \cdots & \\ g(\vec{r}_1, \vec{r}_{Q:s})g(\vec{r}_1, \vec{r}_{Q:r}) & g(\vec{r}_2, \vec{r}_{Q:s})g(\vec{r}_2, \vec{r}_{Q:r}) & \cdots & g(\vec{r}_P, \vec{r}_Q \end{pmatrix} \tag{10}$$

It is interesting to note, from (10), the curves satisfying

$$g(\vec{r}, \vec{r}_s)g(\vec{r}, \vec{r}_r) = c \tag{11}$$

(i.e. rows of J) can be generated for different constants c which depict isocurves (or isosurfaces) with respect to the sensitivity to specific parameter perturbations. For certain special cases, we have plotted the iso-sensitivity curves and surfaces in the Appendix.

In order to decompose the matrix in (10), the approach developed by Nelson and Kahana is applied [23]. First, we assume that there exists two sets of orthogonal basis functions, one for the spatial domain where the unknown parameters are located, i.e. the parameter space, and one for the space where the source/receiver antennas are located, i.e. the excitation space. We denote the orthonormal basis for the parameter space as $\{\varphi_i(\vec{r}_\tau)\}$ and the orthonormal basis for the excitation space as $\{\phi_i(\vec{r}_s, \vec{r}_r)\}$. Thus, we can expand each element of the matrix in (10) into the form

$$g(\vec{r}_\tau, \vec{r}_{\nu:s})g(\vec{r}_\tau, \vec{r}_{\nu:r}) = \sum_{m=0}^{\infty}\sum_{n=0}^{\infty} \lambda_m^n \varphi_m(\vec{r}_\tau)\phi_n(\vec{r}_{\nu:s}, \vec{r}_{\nu:r}) \tag{12}$$

where λ_m^n are the coefficients.

Once again, all (m,n) pairs are denoted by a single index, κ, such that abs(λ_κ) are sorted in non-decreasing order. Assuming the summation over the first K terms of the expansion is sufficiently accurate to represent the original function, the truncated expansion is then written as

$$g(\vec{r}_\tau, \vec{r}_{\nu:s})g(\vec{r}_\tau, \vec{r}_{\nu:r}) \approx \sum_{\kappa=1}^{K} \lambda_\kappa \varphi_{\kappa:m}(\vec{r}_\tau)\phi_{\kappa:n}(\vec{r}_{\nu:s}, \vec{r}_{\nu:r}) \tag{13}$$

Nelson and Kahana [23], [27] demonstrated that once the expansion in (13) is constructed, matrix J can be decomposed into the form

$$J = F\Lambda H^T \tag{14}$$

where

$$F = \begin{pmatrix} \phi_{1:n}(\vec{r}_{1:s}, \vec{r}_{1:r}) & \phi_{2:n}(\vec{r}_{1:s}, \vec{r}_{1:r}) & \cdots & \phi_{K:n}(\vec{r}_{1:s}, \vec{r}_{1:r}) \\ \phi_{1:n}(\vec{r}_{2:s}, \vec{r}_{2:r}) & \phi_{2:n}(\vec{r}_{2:s}, \vec{r}_{2:r}) & \cdots & \phi_{K:n}(\vec{r}_{2:s}, \vec{r}_{2:r}) \\ \cdots & \cdots & \cdots & \cdots \\ \phi_{1:n}(\vec{r}_{Q:s}, \vec{r}_{Q:r}) & \phi_{2:n}(\vec{r}_{Q:s}, \vec{r}_{Q:r}) & \cdots & \phi_{K:n}(\vec{r}_{Q:s}, \vec{r}_{Q:r}) \end{pmatrix} \tag{15}$$

$$\Lambda = \begin{pmatrix} \lambda_1 & 0 & \cdots & 0 \\ 0 & \lambda_2 & \cdots & 0 \\ \cdots & \cdots & \cdots & \cdots \\ 0 & 0 & \cdots & \lambda_K \end{pmatrix} \tag{16}$$

$$H = \begin{pmatrix} \varphi_{1:m}(\vec{r}_1) & \varphi_{2:m}(\vec{r}_1) & \cdots & \varphi_{K:m}(\vec{r}_1) \\ \varphi_{1:m}(\vec{r}_2) & \varphi_{2:m}(\vec{r}_2) & \cdots & \varphi_{K:m}(\vec{r}_2) \\ \cdots & \cdots & \cdots & \cdots \\ \varphi_{1:m}(\vec{r}_P) & \varphi_{2:m}(\vec{r}_P) & \cdots & \varphi_{K:m}(\vec{r}_P) \end{pmatrix} \tag{17}$$

The dimensions of these matrices are: $K \times K$ for Λ, $Q \times K$ for F and $P \times K$ for H where K is the truncation level, Q is the combination number for all source/receiver pairs and P is the total number of unknown parameters. Moreover, the matrices F and H are both (approximately) column orthogonal, i.e. $F^T F = H^T H = I$ which is readily proven from the orthonomalities of the associated basis functions.

Nelson and Kahana also demonstrated in [23] that there exists an orthogonal matrix S such that

$$J = (FS)(S^T \Lambda S)(HS)^T \tag{18}$$

where $S^T \Lambda S$ is a non-negative-valued diagonal matrix. By letting

$$\begin{aligned} U &= FS \\ \Sigma &= S^T \Lambda S \\ V &= HS \end{aligned} \tag{19}$$

equation (18) becomes the SVD of the Jacobian matrix. From (19) we can see that the left and right singular vectors are linear combinations of the basis functions in the excitation space and parameter space, respectively.

From this derivation, it is clear that determining the orthonormal bases of the parameter and excitation spaces is essential for the decomposition of the Jacobian matrix. Unfortunately, it is quite difficult to construct such basis functions for arbitrary spatial domains. In the following section, we focus on a special 2D case because of its practical importance: a circular parameter domain with an equispaced circular source/receiver array.

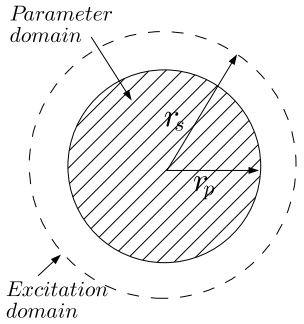

Fig. 1. Circular imaging domain with equally spaced circular antenna array.

C. Jacobian SVD over a circular parameter domain

The problem analyzed in this section is illustrated in Figure 1. The parameter domain is a circular region with radius r_p. Sources and receivers are equally distributed along a concentric circle whose radius is $r_s \geq r_p$. The orthonormal basis functions for a circular parameter domain are the Zernike polynomials [28], [29] which are defined as

$$Z_m^n(\rho, \theta) = R_m^n(\rho / r_p) \exp(jn\theta) \tag{20}$$

where the radial component $R_m^n(\rho)$ is given by

$$R_m^n(\rho) = \sum_{l=0}^{(m-n)/2} \frac{(-1)^l (m-l)!}{l!((m+n)/2-l)!((m-n)/2-l)!} \rho^{m-2l} \tag{21}$$

Thus, H in (17) can be written as

$$H = \begin{pmatrix} \beta_1 Z_{1:m}(\vec{r}_1) & \beta_2 Z_{2:m}(\vec{r}_1) & \cdots & \beta_K Z_{K:m}(\vec{r}_1) \\ \beta_1 Z_{1:m}(\vec{r}_2) & \beta_2 Z_{2:m}(\vec{r}_2) & \cdots & \beta_K Z_{K:m}(\vec{r}_2) \\ \cdots & \cdots & \cdots & \cdots \\ \beta_1 Z_{1:m}(\vec{r}_P) & \beta_2 Z_{2:m}(\vec{r}_P) & \cdots & \beta_K Z_{K:m}(\vec{r}_P) \end{pmatrix} \tag{22}$$

where β_κ is defined by

$$\beta_\kappa = \frac{1}{\sqrt{|Z_\kappa|}} \tag{23}$$

and $|Z_\kappa| = \sqrt{\int Z_\kappa^2(\vec{r}) d\vec{r}}$ is the l^2-norm of the κ-th Zernike polynomial.

Given the orthogonal expansion expression (13), the relationship

$$\lambda_{\kappa:n} \phi_{\kappa:n}(\theta_{\nu:s}, \theta_{\nu:r}) = \frac{1}{|Z_{\kappa:n}|} \int g(\vec{r}, \vec{r}_{\nu:s}) g(\vec{r}, \vec{r}_{\nu:r}) Z_{\kappa:n}(\vec{r}) d\vec{r} \tag{24}$$

holds. If ΛH^T in (14) is denoted by W, then (24) represents the (ν, κ)-th element of matrix W. By considering $H^T H = I$, the singular values λ can finally be computed from

$$\lambda_{\kappa:n} = \sqrt{||w_i||_2} \tag{25}$$

where w_i is the i-th row of matrix W.

The Green's function in the 2D homogeneous case is given by

$$g(\vec{r}, \vec{r'}) = \frac{j}{4} H_0^{(1)}(k_0 |\vec{r} - \vec{r'}|) \tag{26}$$

with $H_0^{(1)}$ being the 0-th order Hankel function of the first kind. By inserting (26) into (24), the integration on the RHS involves the multiplication of three special functions

$$\begin{aligned} \lambda_{\kappa:n} \phi_{\kappa:n}(\theta_{\nu:s}, \theta_{\nu:r}) &= \tfrac{-1}{16|Z_{\kappa:n}|} \\ &\times \int H_0^{(1)}(k_{bk} |\vec{r} - \vec{r}_{\nu:s}|) H_0^{(1)}(k_{bk} |\vec{r} - \vec{r}_{\nu:r}|) Z_{\kappa:n}(\vec{r}) d\vec{r} \end{aligned} \tag{27}$$

The possibility of analytically evaluating this integral is still under investigation; however, here a numerical solution is used to verify our analysis.

In the previous derivation, we assumed that the mesh had uniform sampling density within the parameter domain. We have constructed a parameter mesh meeting this criterion with a radius of 6 cm which is surrounded by a 7.6 cm radius antenna array consisting of 32 equally spaced antennas. Each antenna transmits a signal at 900 MHz while the remaining 31 antennas act as receivers. The Jacobian matrix in this scheme is calculated using our nodal adjoint formula (5) and its SVD is numerically computed. Several right singular vectors were selected as examples whose values are plotted as distributions over the parameter mesh (Figure 2). From these plots, the Zernike polynomials Z_4^4, Z_4^{-4}, Z_4^0, Z_3^1, Z_5^{-3}, Z_5^3, Z_6^0, Z_6^2 and Z_6^4 can be identified as the major component of each pattern as expected.

III. Results

Analytical decomposition of the Jacobian matrix is only available in special cases and evaluation of the integration in (24) is difficult in general. Alternatively, numerical evaluation

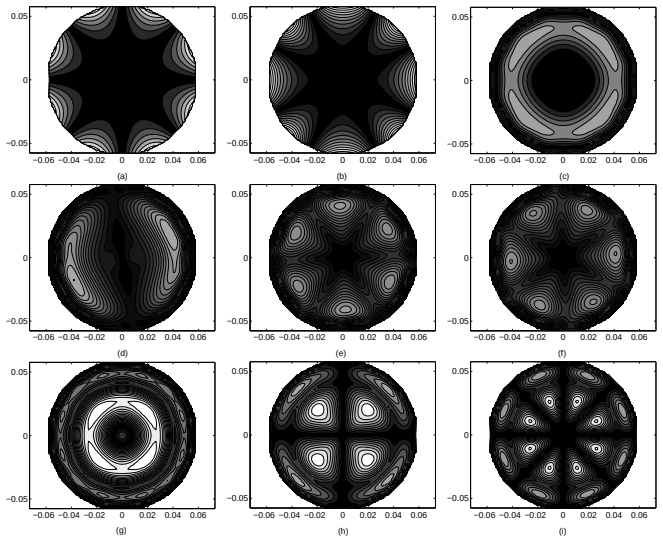

Fig. 2. Magnitude contour plots of right singular vector patterns: (a) $|v_8|$, (b) $|v_9|$, (c) $|v_{28}|$, (d) $|v_{29}|$, (e) $|v_{35}|$, (f) $|v_{36}|$, (g) $|v_{46}|$, (h) $|v_{54}|$, (i) $|v_{65}|$.

of the Jacobian matrix for a homogeneous background can be easily computed even for irregular-shaped parameter domains and source distributions given the nodal adjoint representation in (5). In this section, we study the impact of various imaging parameters, including operating frequency, source/receiver number, domain sizes, background properties and parameter mesh density, on the singular spectrum of the Jacobian matrix, and, consequently, the potential quality of the reconstructed image. Note that the impact of these parameters on the convergence rate, solution stability and solution error were not studied here.

The problem configuration used here is identical to that described in the previous section except where otherwise noted. The numerical singular spectrum of the Jacobian matrices were computed using different system parameters. In order to compare different spectra, we modified the concept of the "degree of ill-posedness" discussed in [17] using the following definition:

Definition 1 (The degree of ill-posedness): if there exists a positive real number α, for a singular spectrum $\{\sigma_i\}_i^N$, and if $\frac{\sigma_i}{\sigma_1} = O(\exp(-\alpha i))$, then, α is called the degree of ill-posedness of the spectrum.

In practices, due to system noise and limited measurement, to compute the degree of ill-posedness in asymptotic means is not possible. In all examples presented in this section, a linear regression was performed on the series $\{\log(\sigma_i) - \log(\sigma_1)\}_i^N$ (N is the numerical rank of the Jacobian) where the slope was used to estimate α.

We first computed the Jacobian singular spectra at various signal frequencies within the working range of our hardware system [30], i.e. 100 MHz to 3000 MHz in 100 MHz increments. A log plot of these curves is shown in Figure 3 (a). The portion of the curves below roughly -14 (log scale) is essentially zero with respect to the compute precision and has been neglected. From the curve in Figure 3 (b), we can see that the degree-of-illposedness at 3000 MHz is roughly 1/3 of that at 100 MHz indicating that higher frequencies provide less redundant information about the target. However, one should recognize that with the increase in frequency, the nonlinearity between the measurement data and dielectric properties becomes more extant requiring a more accurate initial estimate.

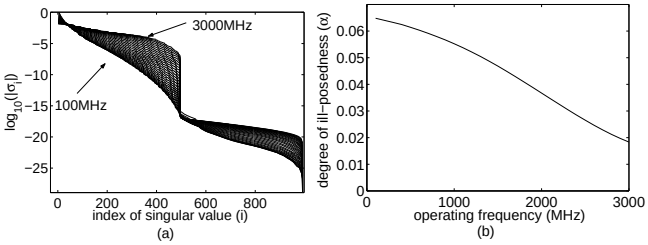

Fig. 3. (a) Singular spectra and (b) degree-of-illposedness as a function of frequency. Note that all Jacobian matrices in this example have rank 496 which is the amount of non-reciprocal measurement data for this case.

In a second experiment, we varied the numbers of sources/receivers surrounding the parameter domain. The antennas were evenly distributed within the array. At 1100 MHz, their spectra for source numbers ranging from 6 to 60 are plotted in Figure 4 (a). The corresponding degree-of-illposedness plot is shown as the solid line in Figure 4 (b) along with those for 700 and 1500 MHz, respectively. These results confirm our experience that more sources can provide more information with the degree-of-illposedness being significantly reduced for higher numbers of antennas. For all three frequencies, the rate of reduction in ill-posedness slows considerably for an antenna array count of 35 or more. Figure 4 (b) also demonstrates the impact of operating frequency as we observed in the first test. In these cases, the higher operating frequency appears to have the most significant benefit for antenna numbers roughly in the range of 8 to 24. An alternative is to plot the degree-of-illposedness versus the reciprocal of the source spacing electrical length for different frequencies which is shown in Figure 5. This plot reveals significant differences between frequencies implying that the source number and operating frequency are more dominant parameters than the antenna spacing in this situation.

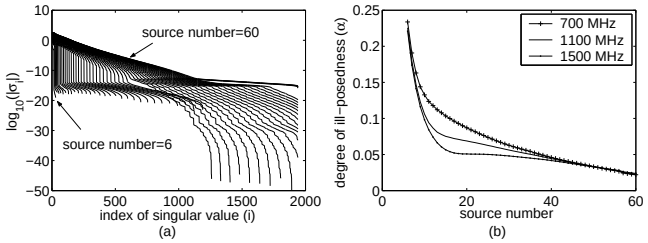

Fig. 4. (a) Singular spectra computed at 1100 MHz for a range of source/receiver numbers, and (b) the degree-of-illposedness as a function of source/receiver for three frequencies.

In the third experiment, we studied the effects of imaging domain sizes. For the circular array configuration (as shown in Figure 1), we computed the degree-of-illposedness over a range of source array radii. The plots at 700 MHz, 1100 MHz and 1500 MHz are shown in Figure 6. For all three frequencies, the degree-of-illposedness increases when the

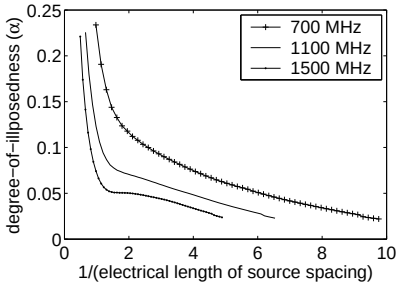

Fig. 5. The degree-of-illposedness as a function of the inverse of source spacing electrical length.

radius of the antenna array expands. This result is consistent with previous phantom results which showed overall improved performance for smaller diameter arrays [31].

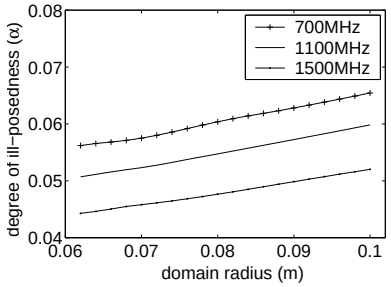

Fig. 6. The degree-of-illposedness for various source array radii.

The fourth experiment focused on the effects of the background medium properties. Utilizing 32 antennas operating at 1100 MHz, we varied the background dielectric properties linearly from air to 0.9% saline ($\epsilon_r = 77$, $\sigma = 1.7$ S/m). The singular spectrum curves are plotted in Figure 7 (a) while the corresponding degree-of-illposedness is shown in Figure 7 (b). These plots demonstrate that a more lossy background medium (in most coupling media we have used in our system, the lossier medium often had higher permittivity as well) produces a lower degree-of-illposedness although the overall effect is relatively modest. Further, the SNR of the measurement drops significantly in very lossy media which has a negative effect on the reconstruction. Therefore, when choosing the background medium, both factors should be considered.

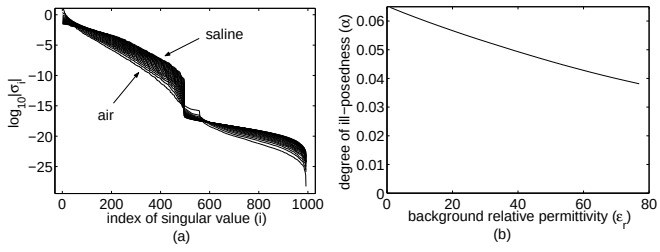

Fig. 7. (a) Singular spectra and (b) degree-of-illposedness for various background media.

The fifth experiment considered the density of the reconstruction mesh, or number of property parameter unknowns. Here, we varied the cell sizes of the reconstruction mesh and computed the corresponding Jacobian singular spectrum. The corresponding singular spectrum and degree-of-illposedness are shown in Figures 8 (a) and (b), respectively. From these curves, we can make three basic observations: 1) if the number of unknowns is less than the amount of non-reciprocal measurement data (equal to the number of sources multiplied by the number of receivers per source divided by two due to reciprocity), the singular spectrum drops precipitously at the number of parameter nodes; 2) when the number of the unknowns is greater than the number of non-reciprocal measurements (i.e. underdetermined cases), the point where the spectrum drops is determined by the amount of measurement data; and 3) increasing the reconstruction mesh density is helpful in reducing the degree-of-illposedness of the problem; however, the significance of this reduction is diminished when the number of unknowns is greater than roughly 2-3 times the amount of non-reciprocal measurement data (in this case, the amount of non-reciprocal measurement data is $\frac{32\times31}{2} = 496$).

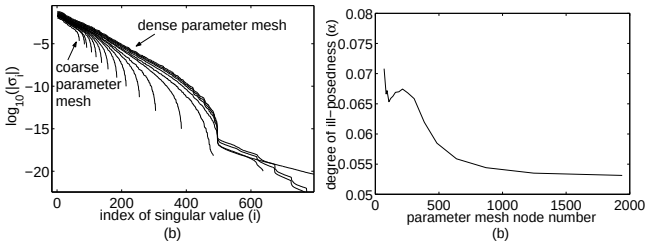

Fig. 8. (a) Singular spectra and (b) degree-of-illposedness for various parameter densities.

In the sixth experiment, we investigated the impact of using multi-frequency data in the dispersion reconstruction technique discussed in [32]. To accomplish this, we repeated the second experiment while incorporating two (700/1100 MHz) and three (300/700/1100 MHz) frequency data sets. The degree-of-illposedness curves were plotted in comparison with that of the single frequency case (1100 MHz) in Figure 9. From the plot, the reduction in α is roughly 20 to 30% on average. This indicates that the amount of non-reciprocal data increases when incorporating multi-frequency data into the reconstruction. In this case, the curve for the three frequency Jacobian has little difference from that generated from the dual-frequency data indicating diminished improvement when adding the lowest (300 MHz) frequency.

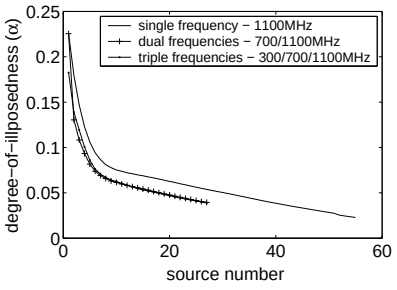

Fig. 9. Degree-of-illposedness for source/receiver numbers computed with different frequency combinations.

One final experiment compared the log-magnitude phase

form (LMPF) and traditional complex code reconstructions. As demonstrated in [33], the LMPF uses a real-valued Jacobian matrix whereas the latter is equivalent to the complex form Jacobian except that the property updates are real variables. The singular spectra of these two Jacobians are exactly the same which demonstrates that the log-magnitude/unwrapped phase transform does not alter the singular spectrum of the Jacobian matrix as expected.

The previous discussion does not take into account measurement noise which is a non-negligible consideration in real applications. The presence of measurement noise essentially sets a truncation level above the matrix numerical rank in the singular spectrum and the maximum extent of the effective spectrum is consequently constrained by this noise level. In Hansen's work [17], a metric termed the "effective resolution limit" is devised to denote the turning point along the singular spectrum where the measurement noise begins to dominate the solution. From the analysis above, the maximum extent of the effective spectrum is directly related to the resolution in the final image and is evident from the orthogonal decomposition expression (12). In general, the more singular spectrum values that are included in the reconstruction, the more Zernike polynomials will be used to construct the solution with correspondingly improved image resolution. This conclusion holds not only for a Jacobian matrix utilizing the Born approximation (single iteration cases), but also for iterative reconstructions. Assuming smooth convergence in an iterative reconstruction, the final image resolution is related to the maximum angular and radial modes of the Zernike polynomials that correspond to the full effective spectrum for all iterations. These high order angular and radial modes are directly constrained by the noise level in the measurements.

IV. Discussions and conclusions

We analyzed the singular value decomposition of the single-iteration Jacobian matrix constructed from a discrete adjoint expression where the contribution to a matrix element is compactly represented as a sum over an effective nodal volume and its associated source-receive fields. The analysis provides insight into the structure of the Jacobian matrix and allows its influence on the reconstruction process to be evaluated. We focused on 2D cases with a homogeneous background, however, the approach can be readily extended to 3D. We used the degree of ill-posedness which is a measure of the decay rate in the singular spectrum of the Jacobian as a convenient metric to compare expected imaging performance as a function of signal frequency, antenna array density and diameter, property parameter sampling, and background properties in a representative imaging geometry. The results suggest substantial gains with increasing signal frequency (monotonic improvement to $\frac{1}{3}$ of the 0.1GHz value at 3GHz) and antenna array density (up to about 35 equally-spaced circumferentially placed elements) but more modest effects with changes in background properties and antenna array diameters. Increasing the number of property estimates (to 2-3 times the amount of measurement data) and adding multi-frequency recordings also offer important benefits in terms of reducing the degree of ill-posedness. While these results were generated under the idealized conditions of no measurement noise, the effect of noise in the data can be accommodated in the analysis by adjusting the low-end threshold for the acceptable singular values which is not expected to dramatically alter the relative relationships between the spectral decay rates that were used as the basis for comparison. Certainly, SNR is an important consideration when extrapolating the findings from this paper (e.g. the desired increase in operating frequency, antenna element density and background loss) to a practical hardware installation. Nonetheless, the results reported here should serve as important guidelines in the development of optimized microwave imaging system designs.

Appendix

Iso-sensitivity ovals and surfaces

A single row of the Jacobian matrix represents the sensitivity map across the imaging domain for a given transmit/receive antenna pair with respect to perturbations of the parameters at different locations. For microwave imaging, this sensitivity map can be expressed through the multiplication of two Green's functions of the Helmholtz equation, i.e.

$$J((\vec{r}_s, \vec{r}_r), \vec{r}) = g(\vec{r}, \vec{r}_s) g(\vec{r}, \vec{r}_r) \tag{28}$$

and the iso-sensitivity curve (in 2D) or surface (in 3D) is defined by

$$g(\vec{r}, \vec{r}_s) g(\vec{r}, \vec{r}_r) = c \tag{29}$$

where c is a constant. For different c values, the curves defined by (29) comprise a contour plot which illustrates the measurement sensitivity over space. We present two examples here. The first is a homogeneous medium in 2D. In this case, the Green's function is written as

$$g(\vec{r}, \vec{r}_s) = \frac{j}{4} H_0^{(1)}(k_0 |\vec{r} - \vec{r}_s|) \tag{30}$$

where k is the complex wave number, and the iso-sensitivity curve is defined by

$$H_0^{(1)}(k_0 |\vec{r} - \vec{r}_s|) H_0^{(1)}(k_0 |\vec{r} - \vec{r}_r|) = c \tag{31}$$

If $\vec{r}_s = (7, 0)$ cm, $\vec{r}_r = (-7, 0)$ cm, and $\epsilon_r = 77, \sigma = 1.7$ S/m are the dielectric properties of the background, the sensitivity contour plot is shown in Figure 10 a.

Similarly, for an infinitely large homogeneous medium in 3D, the corresponding Green's function is

$$g(\vec{r}, \vec{r}_s) = \frac{\exp jk|\vec{r} - \vec{r}_s|}{4\pi |\vec{r} - \vec{r}_s|} \tag{32}$$

We computed the iso-sensitivity surfaces for the case where $\vec{r}_s = (7, 0, 0)$ cm and $\vec{r}_r = (-7, 0, 0)$ cm with the same electrical properties in the background which are shown in Figure 10 b.

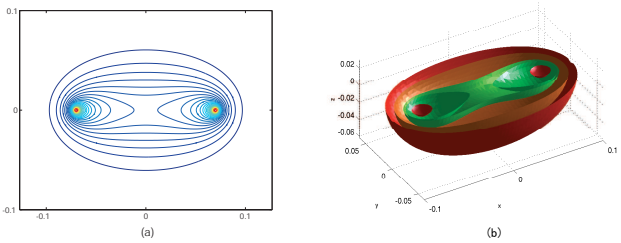

Fig. 10. Iso-sensitivity curves (or surfaces) for an infinitely large (a) 2D and (b) 3D homogeneous background medium.

REFERENCES

[1] W. C. Chew. *Waves and Fields in Inhomogeneous Media*. New York: Van Nostrand-Reinhold, 1990.

[2] A. C. Kak and M. Slaney, editors. *Principles of Computerized Tomographic Imaging*. Society of Industrial and Applied Mathematics, 2001.

[3] W. C. Chew and Y. M. Wang. Reconstruction of two-dimensional permittivity distribution using the distorted Born iterative method. *IEEE Transactios on Medical Imaging*, 9(2):218–225, Jun 1990.

[4] A. Roger. A Newton-Kantorovich algorithm applied to an electromagnetic inverse problem. *IEEE Trans. Antennas Propag.*, 29:232–238, 1981.

[5] N. Joachimowicz, C. Pichot, and J. P. Hugonin. Inverse scattering: an iterative numerical method for electromagnetic imaging. *IEEE Transactions on Antennas and Propagation*, 39:1742–1752, 1991.

[6] R. F. Remis and P. M. van den Berg. On the equivalence of the Newton-Kantorovich and distorted Born methods. *Inverse Problems*, 16(1):L1–L4, Feb 2000.

[7] L. E. Larsen and J. H. Jacobi. Microwave scattering parameter imagery of an isolated canine kidney. *Med Phys*, 6:394–403, 1979.

[8] R. Pethig. Dielectric properties of biological materials: biophysical and medical appliications. *IEEE Trans. on Elec. Insulation*, 19:453–474, Oct 1984.

[9] J. C. Bolomey, J. Izadnegahdar, L. Jofre, C. H. Pichot, G. Peronnet, and M. Solaimani. Microwave diffraction tomography for biomedical applications. *IEEE Trans. Microwave Theory Tech.*, 30:1990–2000, 1982.

[10] C. Pichot, L. Jofre, Peronnet G., and J. Bolomey. Active microwave imaging of inhomogeneous bodies. *IEEE Transactions on Antennas and Propagation*, 33(4), Apr 1985.

[11] A. Broquetas, J. Romeu, J. M. Rius, A. R. Elias-Fuste, A. Cardama, and L. Jofre. Cylindrical geometry: a further step in active microwave tomography. *IEEE Transactions on Microwave Theory and Techniques*, 39(5), May 1991.

[12] P. M. Meaney, K. D. Paulsen, and T. P. Ryan. Two-dimensional hybrid element image reconstruction for TM illumination. *IEEE Trans. Antennas Propagat.*, 43:239–247, 1995.

[13] S. Y. Semenov, R. H. Svenson, A. E. Boulyshev, A. E. Souvorov, V. Y. Borisov, Y. Sizov, A. N. Starostin, K. R. Dezern, G. P. Tatsis, and V. Y. Baranov. Microwave tomography: two-dimensional system for biological imaging. *IEEE Transactions on Biomedical Engineering*, 43(9):869–877, Sep 1996.

[14] P. M. Meaney, M. W. Fanning, D. Li, S. P. Poplack, and K. D. Paulsen. A clinical prototype for active microwave imaging of the breast. *IEEE Trans. Microwave Theory Tech.*, 48:1841–1853, 2000.

[15] Q. H. Liu, Z. Q. Zhang, T. T. Wang, J. A. Bryan, G. A. Ybarra, L. W. Nolte, and W. T. Joines. Active microwave imaging. I. 2-D forward and inverse scattering methods. *IEEE Trans. Microwave Theory Tech.*, 50:123–133, 2002.

[16] G. Strang. *Linear Algebra and its Applications, 3rd ed.* Saunders, Philadelphia, PA, 1988.

[17] P. C. Hansen. *Rank-Deficient and Discrete Ill-Posed Problems: Numerical Aspects of Linear Inversion*. SIAM, Philadelphia, 1997.

[18] G. H. Golub and C. H. van Loan. *Matrix Computations*. The Johns Hopkins University Press, Baltimore, MD, 1991.

[19] O. Brander and B. DeFacio. The role of filters and the singular-value decomposition for the inverse Born approximation. *Inverse Problem*, 2:375–393, 1986.

[20] M. Hori. Inverse analysis method using spectral decomposition of Green's function. *Geophysical Journal International*, 147:77–87, September 2001.

[21] O. M. Bucci and G. Franceschetti. On the degrees of freedom of scattered fields. *IEEE Tran. on Antennas and Propag.*, 37:918–926, 1989.

[22] O. M. Bucci and T. Isernia. Electromagnetic inverse scattering: Retrievable information and measurement strategies. *Radio Science*, 32:2123–2138, 1997.

[23] P. A. Nelson and Y. Kahana. Spherical harmonics, singular value decomposition and the head related transfer function. *Special edition of the Journal of Sound and Vibration*, 239(4):607–637, 2001.

[24] Q. Fang, P. M. Meaney, and K. D. Paulsen. Viable three-dimensional microwave imaging, theory and experiments. *IEEE Trans. Medical Imaging*, page Submitted, 2005.

[25] Q. Fang, P. M. Meaney, S. D. Geimer, and and K. D. Paulsen A. V. Streltsov. Microwave image reconstruction from 3D fields coupled to 2D parameter estimation. *IEEE Trans. Med. Imag.*, 23:475–484, Apr 2004.

[26] J. M. Lee. *Introduction to Topological Manifolds*. Springer-Verlag New York, 2000.

[27] P. A. Nelson and S. H. Yoon. Estimation of acoustic source strength by inverse methods: Part I, Conditioning of the inverse problem; Part II, experimental investigation of methods for choosing regularisation parameters. *Journal of Sound and Vibration*, 233(4):639–701, 2000.

[28] F. Zernike. Beugungstheorie des Schneidenverfahrens und seiner verbesserten Form, der Phasenkontrastmethode. *Physica*, 1:689–704, 1934.

[29] M. Born and E. Wolf. *Principles of Optics: Electromagnetic Theory of Propagation Interference, and Diffraction of Light,6th ed.* New York: Pergamon Press, 1989.

[30] D. Li, P. M. Meaney, T. Raynolds, S. A. Pendergrass, M. W. Fanning, and K. D. Paulsen. A parallel-detection microwave spectroscopy system for breast imaging. *Review of Scientific Instruments*, 75(7):2305–2313, 2004.

[31] P. M. Meaney, K. D. Paulsen, S. Geimer, S. Haider, and M. W. Fanning. Quantification of 3D field effects during 2D microwave imaging. *IEEE Trans. on Biomed. Eng.*, 49:708–720, 2002.

[32] Q. Fang, P. M. Meaney, and K. D. Paulsen. Microwave Image Reconstruction of Tissue Property Dispersion Characteristics Utilizing Multiple Frequency Information. *IEEE Trans. Microwave Techniques and Technology*, 52:1866–1875, Aug 2004.

[33] K. D. Paulsen P. M. Meaney, B. W. Pogue, and M. I. Miga. Microwave image reconstruction utilizing log-magnitude and unwrapped phase to improve high-contrast object recovery. *IEEE Transactions on Medical Imaging*, 20:104–116, 2001.

Qianqian Fang (S'03-M'05) was born in Anyang, Henan, China, in 1976. He received B.Eng. degree in electrical engineering from the University of Electronic Science and Technology of China (UESTC), Chengdu, Sichuan, China, in 1999, and Ph.D. degree in biomedical engineering at Thayer School of Engineering, Dartmouth College, Hanover, USA, in 2005. He is currently a research fellow at Martinos Center for Biomedical Imaging, Massachusetts General Hospital, USA.

From 1999 to 2000, he was a Research Assistant at Computational Electromagnetics Lab, UESTC, and implemented Finite Difference-Time Domain (FDTD) and absorption boundary condition for electromagnetic pulse well-logging. From 2000 to 2004, he was a Research Assistant in microwave imaging group at Dartmouth College, focusing on three-dimensional microwave imaging, FDTD technique and phase unwrapping. He has been a Postdoctoral Research Fellow at Massachusetts General Hospital since early 2005. His current research interests include diffuse optical tomography for breast cancer detection and optical-mechanical modeling of breast under compressions.

Paul M. Meaney (M'92) received A.B.'s in Computer Science and Electrical Engineering from Brown University in 1982, an M.S. in Electrical Engineering from the University of Massachusetts in 1985, and his Ph.D. in Biomedical Engineering from Dartmouth College in 1995.

He was a Postdoctoral Fellow at Dartmouth College from 1995-1996 and a NSF-NATO Postdoctoral Fellow at the Royal Marsden Hospital in Sutton, England from 1996-1997. He has been a Research Assistant Professor at Dartmouth College since 1997. His interests include developing microwave imaging for biomedical applications – especially breast imaging and hyperthermia monitoring, along with elastography and various applications of thermal modeling.

Keith D. Paulsen (S'85-M'86) received the B.S. degree in biomedical engineering from Duke University, Durham, NC, in 1981 and the M.S. and Ph.D. degrees in biomedical engineering from Dartmouth College, Hanover, NH, in 1984 and 1986, respectively.

From 1986 to 1988, he was an Assistant Professor in the Electromagnetics Group within the Department of Electrical and Computer Engineering, University of Arizona, Tucson. He is currently a Professor at the Thayer School of Engineering, Dartmouth College and the Director of the Radiobiology and Bioengineering Research Program for the Norris Cotton Cancer Center within the Dartmouth-Hitchcock Medical Center, Lebanon, NH. His research interests include computational methods with particular emphasis on biomedical problems in cancer therapy and imaging, and model-guided surgery.